

Simultaneous control of the Dzyaloshinskii-Moriya interaction and magnetic anisotropy in nanomagnetic multilayers

A.L. Balk (1,2,3), K-W. Kim (1,2), D.T. Pierce (1), M.D. Stiles (1), J. Unguris (1), S.M. Stavis (1)*

((1) Center for Nanoscale Science and Technology, National Institute of Standards and Technology, Gaithersburg, MD (2) Maryland NanoCenter, University of Maryland, College Park, MD (3) National High Magnetic Field Laboratory, Los Alamos National Laboratory, Los Alamos, NM) *Address correspondence to sstavis@nist.gov

We demonstrate Ar^+ irradiation at the 100 eV scale as a technique for spatially tuning the Dzyaloshinskii-Moriya interaction (DMI) in Pt/Co/Pt trilayers. The irradiation energy determines the sign and magnitude of the DMI independently from magnetic anisotropy, allowing us to vary the DMI while holding the coercive field constant. This independence, which we measure by super-resolution magneto-optical Kerr effect microscopy, emphasizes the different physical origins of these effects. We also observe and propose a physical model for a poorly understood peak in domain wall velocity at zero in-plane field in regions of our trilayers with low DMI. Our technique of structuring the DMI enables new fundamental investigations and technological applications in chiral nanomagnetics.

The Dzyaloshinskii-Moriya interaction (DMI) is a chiral energy term which leads to interesting nanomagnetic states¹⁻³ in magnetic materials. Most notable of these are magnetic skyrmions, which are topologically protected quasiparticles, with promising technological applications⁴⁻⁶ and fundamental physical significance.⁷⁻⁹ However, skyrmions only exist as a ground state in certain areas of the phase space of DMI and non-chiral energy terms such as magnetic anisotropy¹⁰ and Zeeman energy.^{3,11} For this reason, previous studies have required careful adjustment of temperature, magnetic field, and sample growth conditions to obtain the combination of energy terms which leads to a skyrmion ground state. Other chirality-dependent magnetic phenomena, such as current driven domain wall motion,¹²⁻¹⁵ helical spin textures,^{16,17} and spin-orbit torque magnetization switching¹⁸⁻²⁰ are also moderated by a competition between the DMI and non-chiral magnetic effects. While a number of methods have been demonstrated for controlling the DMI, such as changing the arrangement of multilayer stacks,^{21,22} sputtering conditions,^{23,24} and interfacial micromagnetic parameters,²⁵ these methods also lead to variations in magnetic anisotropy and exchange interaction, preventing deterministic selection of points in the phase space of micromagnetic energy parameters. Furthermore, such tuning methods must occur during sample growth, requiring separate samples to obtain a range of DMI values. Addressing these limitations, we demonstrate post-growth Ar^+ irradiation at the 100 eV scale as a method to independently tune the sign and magnitude of the DMI, and the coercive field $\mu_0 H_C$, in a single trilayer of a well-studied magnetic system, Pt/Co/Pt. We attribute this DMI tuning to etching of the top Pt layer by the Ar^+ irradiation, which, at the 100 eV energy scale, happens distinctly from the ion-induced disorder of Co/Pt interfaces that modifies²⁶⁻²⁸ interfacial anisotropy and $\mu_0 H_C$.

In this letter, we first describe a method to precisely and rapidly measure the creep velocity of domain walls, and therefore the effective DMI field $\mu_0 H_{DMI}$, in perpendicularly magnetized Pt/Co/Pt trilayers. We then describe how we use low energy Ar^+ irradiation to modify the properties of the trilayers. We demonstrate that we can independently tune $\mu_0 H_{DMI}$ and $\mu_0 H_C$ by varying the irradiation energy and irradiation time (dose) in an informed manner. Analysis of this result emphasizes a previously observed but unexplained dependence of the creep velocity on magnetic field applied along a

hard axis. We find this dependence to be most significant at small values of $\mu_0 H_{DMI}$, and we propose a physical model for this effect.

We measure the DMI by magneto-optical Kerr effect (MOKE) microscopy of the asymmetric expansion of magnetic bubble domains. A non-zero DMI preferentially leads to the formation of Néel walls with chirality depending on the sign of the DMI. As Fig. 1(a) shows and earlier reports describe,^{25,29-31} applied in-plane fields such as B_y then modify the surface tension of these Néel walls, which in turn modifies the velocity of domain walls driven with a field perpendicular to the trilayer surface B_z . The modification to the domain wall velocity depends on the chirality of the domain wall and the direction of the applied field, and indicates the sign and magnitude of the DMI. For bubble domains with consistent domain wall chirality, the nonzero DMI therefore leads to asymmetric expansion of these bubble domains. We use this mechanism to determine the DMI in our ion-irradiated Pt/Co/Pt trilayer. In summary of our results, in low- $\mu_0 H_c$ regions of the trilayer irradiated with 50 eV Ar^+ , applying B_y in the negative y direction causes asymmetric expansion of bubbles with positive M_z in the negative y direction (Fig. 1(b), blue), indicating negative DMI. In low- $\mu_0 H_c$ regions of the trilayer irradiated with 100 eV Ar^+ , applying B_y in the negative y direction causes the asymmetric expansion of bubbles with positive M_z in the positive y direction (Fig. 1(c), blue), indicating positive DMI. The bubbles expand in opposite directions for positive B_y (Fig. 1(b,c), red).

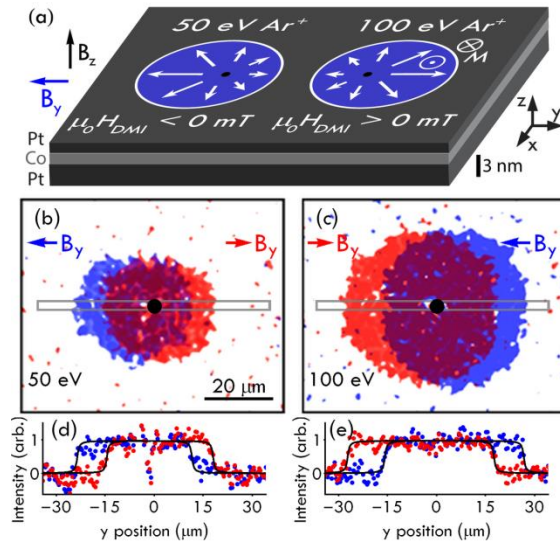


Fig. 1: Irradiation of a Pt/Co/Pt trilayer with Ar^+ at the 100 eV scale tunes the sign of the Dzyaloshinskii-Moriya interaction (DMI). (a) A schematic drawing shows magnetic bubble domains with positive M_z (blue circles) in trilayer regions irradiated with 50 eV Ar^+ or 100 eV Ar^+ , expanding asymmetrically (white arrows) in opposite y directions from nucleation sites (black dots) in response to applied fields B_z and B_y . The doses of Ar^+ irradiation were chosen to make the coercive fields $\mu_0 H_c$ of the two areas approximately the same. (b) A magneto-optical Kerr effect (MOKE) micrograph shows that negative B_y causes a bubble in a trilayer area irradiated with 50 eV Ar^+ to asymmetrically expand in the negative y direction (blue), and positive B_y causes a bubble in the same area to asymmetrically expand in the positive y direction (red). (c) A MOKE micrograph shows that negative B_y causes a bubble in a trilayer area irradiated with 100 eV Ar^+ to asymmetrically expand in the positive y direction (blue) and positive B_y causes a bubble in the same area to asymmetrically expand in the negative y direction (red). Black dots in (a)-(c) indicate the approximate position of bubble nucleation. Gray boxes in (b) and (c) indicate areas

from which we take profiles to determine displacements of domain walls. We have spatially averaged, thresholded, colored, and removed backgrounds from panels (b) and (c) for clarity. (d-e) Profiles from boxed areas in (b) and (c) averaged across the x direction. Negative B_y (blue) and positive B_y (red) results highlight the opposite asymmetry of bubble expansion for the different irradiation energies. Black curves show arctangent fits used to extract the positions of domain walls with standard uncertainties of ≈ 400 nm.

We perform all measurements on a single trilayer of $\text{Pt}_{35\text{ nm}}/\text{Co}_{0.8\text{ nm}}/\text{Pt}_{1.7\text{ nm}}$ sputtered on a p-type silicon wafer (Supplemental Material S1). The $\mu_0 H_C$ of the trilayer as grown is ≈ 60 mT, which is larger than the maximum field of the electromagnet that we use to apply B_z . Therefore, we do not measure the DMI in the trilayer as grown. After trilayer growth, we dice this wafer into smaller chips to systematically investigate the effect of Ar^+ irradiation.

We irradiate areas of the chips with Ar^+ at a range of energies E_{Ar^+} from 50 eV to 140 eV in increments of 5 eV. We use a shadow mask to expose each area to a spatially varying dose of Ar^+ , generating values of $\mu_0 H_C$ ranging from the as-grown value of $\mu_0 H_C \approx 60$ mT to the spin reorientation transition²⁷ where $\mu_0 H_C$ approaches 0 and spontaneous domain fluctuations occur.³² For these trilayers and energies, the spin reorientation transition occurs at Ar^+ ion irradiation doses of $3 \times 10^{15} \text{ cm}^{-2}$ to $7 \times 10^{15} \text{ cm}^{-2}$.

For field excitation perpendicular to the trilayer plane, we apply a bipolar, pulsed waveform of B_z at a repetition frequency of 50 Hz to 150 Hz and at an amplitude of 1 mT to 10 mT (Supplemental Material S2). This B_z waveform induces bubbles at the repetition frequency, which we set to be higher than the 10 Hz frame rate of the imaging sensor. In this way, each image frame is the average of 5 to 15 bubble expansions, reducing the noise of the measurement by averaging over stochastic domain wall pinning. When excited with this B_z waveform, each chip shows nucleation sites at an areal density of $\approx 100 \text{ mm}^{-2}$, enabling measurement of isolated bubbles (Fig. 1(b,c)). Earlier studies²⁵ used more complicated protocols for B_z excitation, based on a nucleation pulse followed by measurement during a propagation pulse to eliminate possible effects due to inconsistent nucleation of bubbles. Here, we use only a single pulse to make the measurement faster. We verify that the results from a single pulse and from two pulses are consistent (not shown).

For field excitation in the plane of the trilayer, we apply B_y in a triangular waveform at a frequency of 50 mHz and an amplitude of 40 mT. This B_y frequency is much lower than the B_z repetition frequency and the imaging frequency of 10 Hz, so that the position of each domain wall accurately indicates the influence of B_y on domain propagation velocity. The bubbles are sensitive to z -direction misalignment of B_y , so we adjust the angle of the trilayer at large values of B_y to eliminate variations in the size of the expanded bubbles. We are able to measure single bubbles consistently at values of B_y up to approximately 20 mT to 40 mT. Higher values of B_y result in an overly high density of nucleation sites.

We extract the two domain wall displacements from the center of each bubble with the MOKE microscope in real time by taking a cross-sectional strip of each bubble (Fig. 1(b,c), grey boxes) and averaging these strips across the x direction to obtain a one-dimensional profile of each bubble (Fig. 1(d,e), markers). We then fit the resulting profiles with a sum of two offset arctangent functions that model the domain walls (Fig. 1(d,e), black lines). This empirical fit is a good approximation of the effects of stochastic domain wall pinning and broadening by optical diffraction. The fit includes only the two domain wall positions as floating parameters to increase measurement speed, enabling the measurement of approximately 400 single bubbles for this study and the detailed mapping of the DMI that we present below. With this fit, we determine domain wall displacements at 10 Hz with a standard uncertainty of approximately 400 nm per frame. We calculate domain wall velocities by dividing the

measured domain wall displacement by the positive B_z pulse duration, resulting in values of $10 \text{ mm}\cdot\text{s}^{-1}$ to $50 \text{ mm}\cdot\text{s}^{-1}$, with typical standard uncertainties of $0.8 \text{ mm}\cdot\text{s}^{-1}$ for each frame.

To perform a measurement, we simultaneously measure domain wall velocities and B_y *in-situ*. However, since the domain wall comprising the bubble has opposite symmetry on either side of the bubble with respect to B_y , the magnetic field in the reference frame of the domain wall $B_{y(\text{eff})}$ is opposite in sign for each side of the bubble. (Fig. 2, inset). Using this definition, we resample the raw data, which includes multiple cycles of B_y , by averaging data points with $B_{y(\text{eff})}$ within 1 mT of each other. We compute the standard uncertainty of these resampled points from the standard deviations of the raw values averaged to create each resampled point. Typical standard uncertainties for the data in Fig. 2 are $0.16 \text{ mm}\cdot\text{s}^{-1}$. With this measurement technique, we find that the domain wall behaves similarly on both sides of the bubble as a function of $B_{y(\text{eff})}$ (Fig. 2). This typical data comes from a region of the trilayer exposed to 125 eV Ar^+ , and is an average of 12 B_y cycles. The similar behavior of the domain wall on both sides of the bubble indicates the preservation of the domain wall's chirality around the bubble, which is typical for all bubbles in this study. We can also rule out the effects of chiral damping with this data, which would emerge as an asymmetry of these curves about their minima (Supplemental Material S3).³³

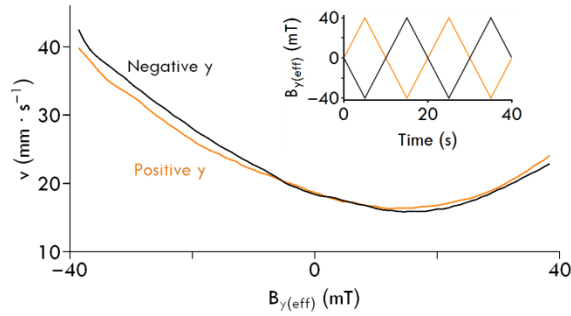


Fig. 2: Representative data shows a simultaneous measurement of the velocities v of a domain wall on the positive y (orange) and negative y (black) sides of a bubble. The domain wall behaves similarly on both sides of the bubble in response to the effective magnetic field $B_{y(\text{eff})}$. We attribute the difference between the curves to a misalignment of B_y which adds a z component to the total field. Typical standard uncertainties as determined by the sampling statistics for each data point are $0.16 \text{ mm}\cdot\text{s}^{-1}$. Inset: $B_{y(\text{eff})}$ is opposite in sign for the domain wall on each side of the bubble, due to the opposite spatial symmetry.

For a systematic study of the DMI in the trilayer, we obtain over 400 separate domain wall velocity curves such as shown in Fig. 2, although averaging over only 2 cycles of B_y . To compare the results from many bubbles which may not have exactly the same expansion velocity, we normalize each domain velocity curve to its velocity at $B_{y(\text{eff})} = 0$, $\tilde{v} = v/v_{(B_{y(\text{eff})}=0)}$. Additionally, we measure the mean \tilde{v} of the domain wall on either side of the bubble, since it behaves similarly with response to $B_{y(\text{eff})}$ (Fig. 2). Typical standard uncertainties of \tilde{v} after such averaging are about 0.01. Finally, after each bubble measurement, we determine the local $\mu_0 H_c$ of the trilayer by measuring a hysteresis loop of the trilayer at the location of the bubble with a ramp rate of B_z of approximately $20 \text{ mT}\cdot\text{s}^{-1}$.

At low in-plane fields, domain walls in perpendicularly magnetized materials show quadratic behavior as a function of applied in-plane field, due to a modification to the domain wall surface tension.³¹ In our data, the quadratic component of each of the domain wall velocity curves has a minimum between the +40 mT and -40 mT B_y limits of the measurement, as shown in the gray fits in Fig.

3. The field locations of these minima determine²⁹ $\mu_0 H_{DMI}$ in the material. While a recent study³⁴ has questioned the quantitative interpretation of the domain wall velocity minimum as a direct indicator of $\mu_0 H_{DMI}$, it should function as a qualitative indicator of the sign and relative magnitude of $\mu_0 H_{DMI}$.

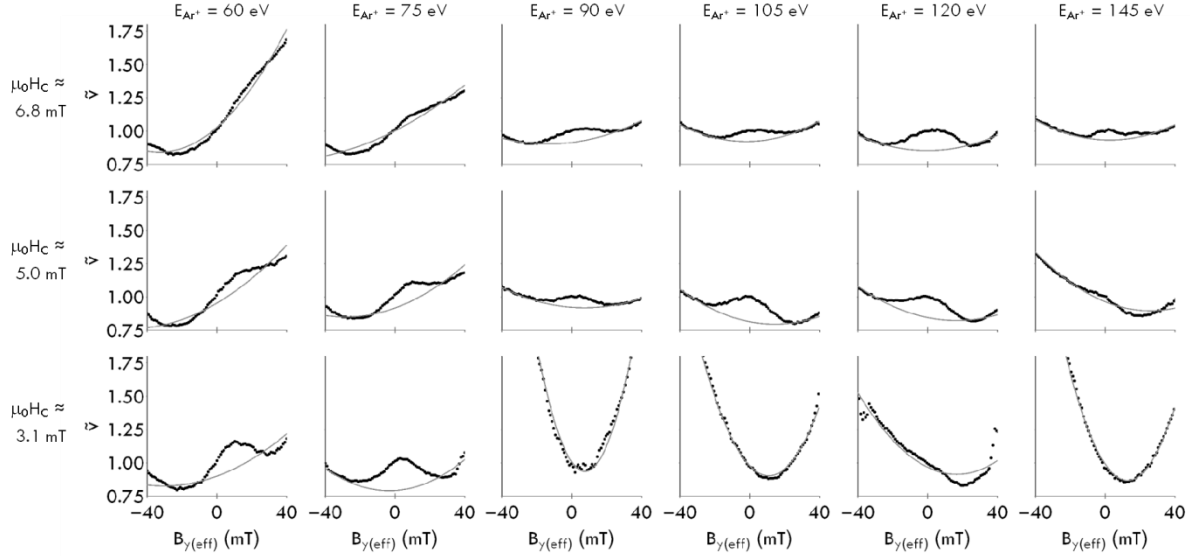


Fig. 3: Representative data shows the normalized domain wall velocity \tilde{v} at three values of the film $\mu_0 H_c$ and six values of Ar^+ irradiation energy E_{Ar^+} . Gray curves are the quadratic fits used to extract the value of $\mu_0 H_{DMI}$. The data at $\mu_0 H_c \approx 5$ mT exemplifies bipolar tuning of $\mu_0 H_{DMI}$ at constant $\mu_0 H_c$. Typical standard uncertainties in this \tilde{v} data are about 0.01, which is smaller than the thickness of the data markers in most cases. The quadratic fit does not capture the central peak in \tilde{v} that occurs near $B_y = 0$ in some of the curves, which we discuss below.

The \tilde{v} curves and corresponding $\mu_0 H_{DMI}$ values show a number of trends as a function of both $\mu_0 H_c$ and E_{Ar^+} (Fig. 3). On regions of the trilayer with $\mu_0 H_c \approx 5.0$ mT (Fig. 3, center row), the quadratic components of the \tilde{v} curves show minima at negative $B_{y(\text{eff})}$ for areas irradiated with low E_{Ar^+} , and minima at positive $B_{y(\text{eff})}$ for regions irradiated with high E_{Ar^+} . Similar trends occur at other values of $\mu_0 H_c$, although the irradiation energy at which the minima transition from negative to positive $B_{y(\text{eff})}$ changes. This is the main result of our study – ion dose and energy independently control $\mu_0 H_{DMI}$ and $\mu_0 H_c$. We also observe a peak in the domain wall velocity at small values of $B_{y(\text{eff})}$, which we discuss below.

To quantify these results, we fit each \tilde{v} curve to determine $\mu_0 H_{DMI}$. We use a multistep fitting algorithm to extract the minimum of the quadratic part of each \tilde{v} curve, despite the presence of a central peak near $B_{y(\text{eff})} = 0$ in some of the curves. We discuss the details of this fit in Supplemental Material S4. The measured values of $\mu_0 H_{DMI}$ have typical standard uncertainties of 1 mT that we derive from the fits, and that are much smaller than most $\mu_0 H_{DMI}$ fields we measure. A plot of the measured minima $\mu_0 H_{DMI}$ as a function of E_{Ar^+} and $\mu_0 H_c$ shows the conditions over which the DMI is tunable (Fig. 4). The regions of positive (green) and negative (purple) $\mu_0 H_{DMI}$ are visible, as is the contour separating the two regions (gray line). Black markers indicate the $\mu_0 H_c$ and E_{Ar^+} of each measurement. Supplemental Material Fig. S5 shows data over an expanded range, with higher and lower $\mu_0 H_c$ values. This result shows tuning of $\mu_0 H_{DMI}$ at constant $\mu_0 H_c$, and post-growth tuning of $\mu_0 H_{DMI}$. As an example of this tuning, this graph shows that a region of a device could be tuned to have $\mu_0 H_c$ of 3.6 mT and $\mu_0 H_{DMI}$ of -20 mT

with exposure to 50 eV Ar^+ , and a different region of the same device could have the same $\mu_0 H_c$ of 3.6 mT but a $\mu_0 H_{DMI}$ of 20 mT with exposure to 100 eV Ar^+ . As a demonstration of this capability, we pattern $\mu_0 H_{DMI}$ on a single chip with the approximate parameters indicated with large black markers in Fig. 4. The effects of positive and negative $\mu_0 H_{DMI}$ are evident with identical B_y and B_z excitation, within the same 250 μm by 190 μm field of view of the MOKE microscope (Supplemental Material Video S6).

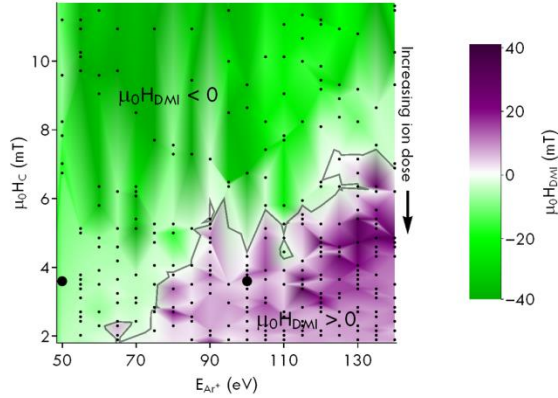


Fig. 4: A surface plot of $\mu_0 H_{DMI}$ shows trends as a function of $\mu_0 H_c$ and E_{Ar^+} . Ion dose increases toward the bottom of this surface plot. The gray contour indicates the boundary between positive and negative $\mu_0 H_{DMI}$. Circular black markers indicate the $\mu_0 H_c$ and E_{Ar^+} values of the measurements between which the color map interpolates. The two large black circular markers indicate the approximate parameters corresponding to Supplemental Material Video S6, which demonstrates this tuning. Standard uncertainties on $\mu_0 H_{DMI}$ derived from fits for the data in this plot have a mean value of approximately 1 mT. Uncertainties for the $\mu_0 H_c$ values are less than 0.25 mT, and are determined by the field sampling rate when performing the hysteresis measurements on the film. Uncertainties of the E_{Ar^+} values are less than 1 eV, as determined by the precision of the energy adjustment mechanism in the ion source. Supplemental Material Fig. S5 shows this data over a larger $\mu_0 H_c$ range.

We propose that our ability to separately tune $\mu_0 H_{DMI}$ and $\mu_0 H_c$ is due to differences in the physical origins of these effects. One possibility is that $\mu_0 H_{DMI}$ is sensitive to the surface coverage of the top Pt interfacial layer³⁵ and insensitive to interface roughness,^{23,24} while $\mu_0 H_c$ is sensitive to the thickness of the top layer of Pt³⁶ and strongly sensitive to interface roughness.³⁷ In this case, we would attribute tuning of $\mu_0 H_{DMI}$ to Ar^+ etching of the top interfacial layer of Pt, which allows the bottom Pt layer to dominate the DMI, similarly to an earlier report,²⁵ and variation in $\mu_0 H_c$ to interfacial disorder from Ar^+ irradiation.³⁸ The energy dependence of the DMI at fixed $\mu_0 H_c$ arises from the vanishing etching rate of Pt at lower Ar^+ energies.³⁹ Namely, the lower-energy Ar^+ ions primarily disorder the interfaces without removing Pt, and the higher energy Ar^+ ions primarily remove Pt without disordering the interfaces. As a result, the $\mu_0 H_{DMI} = 0$ point, at which we have removed only some of the top Pt, occurs with less interface disorder and higher $\mu_0 H_c$ for higher E_{Ar^+} , and more interface disorder and lower $\mu_0 H_c$ for lower E_{Ar^+} . This explains the shape of the $\mu_0 H_{DMI} = 0$ contour (gray line) in Fig. 4. Auger spectroscopy (Supplemental Material S7) shows that the $\mu_0 H_{DMI} = 0$ point occurs when we have removed a fraction of the top Pt, supporting this explanation.

In the data shown in Fig. 3, we also observe a positive peak near $B_{y(\text{eff})} = 0$ for the low $\mu_0 H_{DMI}$ regions of the sample, for example, in the $\mu_0 H_c \approx 3.1$ mT, $E_{\text{Ar}^+} = 75$ eV curve. This peak also occurs in measurements of \tilde{v} in the x direction. Previous studies have reported this central peak,^{23,33,40} ruling out

experimental artifacts from the details specific to our experiment, such as our method of ion irradiation for tuning the DMI and our simplified scheme of single pulses B_z . Rather, we expect a physical origin of the peak.

A possible explanation for the central peak which matches the observed symmetry of the data is a B_y -dependent modification to the prefactor v_0 in the domain wall creep equation, $v = v_0 e^{[-\kappa B_z^{-1/4}]}$. In this equation, v is the domain wall velocity and κ is a quantity related to the domain wall surface tension, pinning potential, and temperature. The value of v_0 depends on the impurity correlation length and the attempt frequency ω of a non-reversed spin comprising a domain wall pinning site.⁴¹ The attempt frequency decreases with a field such as B_y applied along a hard axis of a material.⁴²⁻⁴⁴ This is because a field applied along a hard axis will, on average, move the equilibrium angle θ of a non-reversed spin away from its minimum of anisotropy energy E_{anis} . θ here is defined relative to the surface normal. Since this anisotropy energy minimum corresponds to a maximum of the second derivative of the anisotropy energy, $\frac{d^2}{d\theta^2}[E_{anis}]$ for a sinusoidal anisotropy model, it also corresponds to a maximum in ω . Therefore, any deviation of θ from its value at $B_y = 0$ will decrease ω and thus v_0 , in an amount proportional to $\frac{d^2}{d\theta^2}[E_{anis}]$. With a simple model for the anisotropy energy,⁴⁵ this explanation predicts a peak in \tilde{v} at $B_y = 0$,

$$\tilde{v} \propto v_0 \propto \omega \propto \frac{d^2}{d\theta^2}[E_{anis}] = \frac{d^2}{d\theta^2}[-K_1 \cos^2 \theta - K_2 \cos^4 \theta] = 2[(K_1 + K_2) \cos(2\theta) + K_2 \cos(4\theta)],$$

where, taking the small-angle approximation for the equilibrium angle of the pinned spin:

$$\theta = \frac{MB_y}{2K_1 + MB_z}.$$

In this model, K_1 and K_2 are respectively the first and second order anisotropy constants and M is the saturation magnetization. This model fits the central peak in the data reasonably well (Supplemental Material Fig. S4). For a given in-plane field, θ depends sensitively on K_1 . Therefore, this model predicts that the width of the central peak should scale with K_1 and consequently $\mu_0 H_c$, and that the amplitude of the central peak should scale with K_1^{-2} . We cannot easily separate the effects of the DMI from this central peak to verify these trends, but data from a previous study⁴⁶ is consistent with the second trend, supporting the model. From the model, and estimates of M for ultrathin, amorphous films of CoPt,⁴⁷ we can then extract an estimate for K_1 , which ranges from $1 \times 10^6 \text{ J}\cdot\text{m}^{-3}$ to $2 \times 10^6 \text{ J}\cdot\text{m}^{-3}$. This value overestimates what has been measured⁴⁸ for values of effective anisotropy K_{eff} for samples with similar values of $\mu_0 H_c$ by a factor of 5 to 10. However, we can partially reconcile this discrepancy as the anisotropy measured in this way should only apply to the pinned spins, which should have higher anisotropy than the sample average. Furthermore, bulk observations of K_{eff} should underestimate our measured value of K_1 due to the influence of demagnetization energy, which averages to zero for a moment near a domain wall in our measurements. These observations motivate future measurements of \tilde{v} in the direction mutually perpendicular to the surface normal (z) and applied field (y) directions, which show the effects of a changing v_0 but not DMI, and would enable an estimate of the variation in anisotropy across a sample.

In conclusion, we have demonstrated the use of Ar^+ irradiation at the 100 eV scale to fine-tune the sign and magnitude of the DMI in ultrathin Pt/Co/Pt trilayers. We have shown that the tuning is spatially variable, separately from $\mu_0 H_c$. The observed dependencies are consistent with a model of etching of the top Pt layer modifying the net DMI in the magnetic trilayer. At low values of the DMI, we observe a peak in domain wall velocity which can potentially be explained by a modification of the

depinning attempt frequency in the creep regime of domain wall motion. Our technique for separate tuning of the $\mu_0 H_{DMI}$ and $\mu_0 H_c$ on a single chip will enable systematic study of the effects of the DMI isolated from stronger interactions,⁴⁹ and potentially allows micro and nano-patterning of the DMI. Finally, this degree of control will enable magnetic materials with a predetermined DMI for proposed and existing technological applications.⁵⁰⁻⁵⁴

Acknowledgments

The authors acknowledge Carl Boone, Paul Haney, and J. Alexander Liddle for thoughtful reviews and helpful criticism, and Kerry Siebein for assistance with X-ray diffraction measurements. A.L.B. and K.W.K. acknowledge support of this research under the Cooperative Research Agreement between the University of Maryland and the National Institute of Standards and Technology Center for Nanoscale Science and Technology, Award No. 70NANB10H193, through the University of Maryland.

References

- ¹ M. Heide, G. Bihlmayer, and S. Blügel, Phys. Rev. B **78** (14), 140403 (2008).
- ² G. Chen, J. Zhu, A. Quesada, J. Li, A. N'Diaye, Y. Huo, T. Ma, Y. Chen, H. Kwon, and C. Won, Phys. Rev. Lett. **110** (17), 177204 (2013).
- ³ X. Z. Yu, Y. Onose, N. Kanazawa, J. H. Park, J. H. Han, Y. Matsui, N. Nagaosa, and Y. Tokura, Nature **465** (7300), 901 (2010).
- ⁴ S. Woo, K. Litzius, B. Kruger, M.-Y. Im, L. Caretta, K. Richter, M. Mann, A. Krone, R. M. Reeve, M. Weigand, P. Agrawal, I. Lemesh, M.-A. Mawass, P. Fischer, M. Klaui, and G. S. D. Beach, Nat. Mater. **15** (5), 501 (2016).
- ⁵ A. Fert, V. Cros, and J. Sampaio, Nat. Nanotech. **8** (3), 152 (2013).
- ⁶ W. Jiang, P. Upadhyaya, W. Zhang, G. Yu, M. B. Jungfleisch, F. Y. Fradin, J. E. Pearson, Y. Tserkovnyak, K. L. Wang, and O. Heinonen, Science **349** (6245), 283 (2015).
- ⁷ T. Schwarze, J. Waizner, M. Garst, A. Bauer, I. Stasinopoulos, H. Berger, C. Pfleiderer, and D. Grundler, Nat. Mater. **14** (5), 478 (2015).
- ⁸ W. Jiang, X. Zhang, G. Yu, W. Zhang, M. B. Jungfleisch, J. E. Pearson, O. Heinonen, K. L. Wang, Y. Zhou, and A. Hoffmann, arXiv preprint arXiv:1603.07393 (2016).
- ⁹ X. Yu, A. Kikkawa, D. Morikawa, K. Shibata, Y. Tokunaga, Y. Taguchi, and Y. Tokura, Phys. Rev. B **91** (5), 054411 (2015).
- ¹⁰ H. Kwon, K. Bu, Y. Wu, and C. Won, J. Magn. Magn. Mater. **324** (13), 2171 (2012).
- ¹¹ S. Mühlbauer, B. Binz, F. Jonietz, C. Pfleiderer, A. Rosch, A. Neubauer, R. Georgii, and P. Böni, Science **323** (5916), 915 (2009).
- ¹² A. Thiaville, S. Rohart, É. Jué, V. Cros, and A. Fert, Europhys. Lett. **100** (5), 57002 (2012).
- ¹³ E. Martinez, S. Emori, and G. S. D. Beach, Appl. Phys. Lett. **103** (7), 072406 (2013).
- ¹⁴ K. Ueda, K.-J. Kim, Y. Yoshimura, R. Hiramatsu, T. Moriyama, D. Chiba, H. Tanigawa, T. Suzuki, E. Kariyada, and T. Ono, Appl. Phys. Express **7** (5), 053006 (2014).
- ¹⁵ S. Emori, E. Martinez, K.-J. Lee, H.-W. Lee, U. Bauer, S.-M. Ahn, P. Agrawal, D. C. Bono, and G. S. Beach, Phys. Rev. B **90** (18), 184427 (2014).
- ¹⁶ P. Bak and M. H. Jensen, J. Phys. C: Sol. Stat. Phys. **13** (31), L881 (1980).
- ¹⁷ K. Bu, H. Kwon, S. Kang, H. Kim, and C. Won, J. Magn. Magn. Mater. **343**, 32 (2013).
- ¹⁸ N. Perez, E. Martinez, L. Torres, S. H. Woo, S. Emori, and G. S. D. Beach, Appl. Phys. Lett. **104** (9), 092403 (2014).

19 O. J. Lee, L. Q. Liu, C. F. Pai, Y. Li, H. W. Tseng, P. G. Gowtham, J. P. Park, D. C. Ralph, and R. A.
 Buhrman, Phys. Rev. B **89** (2) (2014).
 20 A. W. Rushforth, Appl. Phys. Lett. **104** (16), 162408 (2014).
 21 H. Yang, O. Boulle, V. Cros, A. Fert, and M. Chshiev, arXiv preprint arXiv:1603.01847 (2016).
 22 G. Chen, T. Ma, A. T. N'Diaye, H. Kwon, C. Won, Y. Wu, and A. K. Schmid, Nat. Comm. **4** (2013).
 23 R. Lavrijsen, D. Hartmann, A. van den Brink, Y. Yin, B. Barcones, R. Duine, M. Verheijen, H.
 Swagten, and B. Koopmans, Phys. Rev. B **91** (10), 104414 (2015).
 24 A. W. Wells, P. M. Shepley, C. H. Marrows, and T. A. Moore, arXiv preprint arXiv:1608.03826
 (2016).
 25 A. Hrabec, N. Porter, A. Wells, M. Benitez, G. Burnell, S. McVitie, D. McGrouther, T. Moore, and
 C. Marrows, Phys. Rev. B **90** (2), 020402 (2014).
 26 C. Chappert, H. Bernas, J. Ferré, V. Kottler, J.-P. Jamet, Y. Chen, E. Cambril, T. Devolder, F.
 Rousseaux, V. Mathet, and H. Launois, Science **280** (5371), 1919 (1998).
 27 N. Bergeard, J.-P. Jamet, J. Ferré, A. Mougin, and J. Fassbender, J. Appl. Phys. **108** (10), 103915
 (2010).
 28 J. Fassbender and J. McCord, J. Magn. Magn. Mater. **320** (3), 579 (2008).
 29 S.-G. Je, D.-H. Kim, S.-C. Yoo, B.-C. Min, K.-J. Lee, and S.-B. Choe, Phys. Rev. B **88** (21), 214401
 (2013).
 30 D.-Y. Kim, D.-H. Kim, J. Moon, and S.-B. Choe, Appl. Phys. Lett. **106** (26), 262403 (2015).
 31 S.-G. Je, D.-H. Kim, S.-C. Yoo, B.-C. Min, K.-J. Lee, and S.-B. Choe, Phys. Rev. B **88** (21) (2013).
 32 A. Balk, M. Stiles, and J. Unguris, Phys. Rev. B **90** (18), 184404 (2014).
 33 E. Jué, C. K. Safeer, M. Drouard, A. Lopez, P. Balint, L. Buda-Prejbeanu, O. Boulle, S. Auffret, A.
 Schuhl, A. Manchon, I. M. Miron, and G. Gaudin, Nat. Mater. **15** (3), 272 (2016).
 34 R. Soucaille, M. Belmeguenai, J. Torrejon, J.-V. Kim, T. Devolder, Y. Roussigné, S.-M. Chérif, A.
 Stashkevich, M. Hayashi, and J.-P. Adam, arXiv preprint arXiv:1604.05475 (2016).
 35 H. Yang, A. Thiaville, S. Rohart, A. Fert, and M. Chshiev, Phys. Rev. Lett. **115** (26), 267210 (2015).
 36 Z. Zhang, P. E. Wigen, and S. S. P. Parkin, J. Appl. Phys. **69** (8), 5649 (1991).
 37 C. Rettner, S. Anders, J. Baglin, T. Thomson, and B. Terris, Appl. Phys. Lett. **80** (2), 279 (2002).
 38 C. Chappert, H. Bernas, J. Ferré, V. Kottler, J.-P. Jamet, Y. Chen, E. Cambril, T. Devolder, F.
 Rousseaux, and V. Mathet, Science **280** (5371), 1919 (1998).
 39 Y. Yamamura and H. Tawara, At. Data Nucl. Data Tables **62** (2), 149 (1996).
 40 Y. Kabanov, Y. Iunin, V. Nikitenko, A. Shapiro, R. Shull, L. Zhu, and C. Chien, IEEE Trans. Magn. **46**
 (6), 2220 (2010).
 41 J. Gorchon, S. Bustingorry, J. Ferré, V. Jeudy, A. B. Kolton, and T. Giamarchi, Phys. Rev. Lett. **113**
 (2), 027205 (2014).
 42 H.-J. Suh, C. Heo, C.-Y. You, W. Kim, T.-D. Lee, and K.-J. Lee, Phys. Rev. B **78** (6), 064430 (2008).
 43 W. F. Brown, Phys. Rev. **130** (5), 1677 (1963).
 44 W. F. Brown Jr, IEEE Trans. Magn. **15** (5), 1196 (1979).
 45 A. Timopheev, R. Sousa, M. Chshiev, T. Nguyen, and B. Dieny, arXiv preprint arXiv:1602.05815
 (2016).
 46 R. Lavrijsen, D. M. F. Hartmann, A. van den Brink, Y. Yin, B. Barcones, R. A. Duine, M. A.
 Verheijen, H. J. M. Swagten, and B. Koopmans, Phys. Rev. B **91** (10) (2015).
 47 M. Charilaou, C. Bordel, P. E. Berche, B. B. Maranville, P. Fischer, and F. Hellman, Phys. Rev. B **93**
 (22), 224408 (2016).
 48 P. J. Metaxas, J. P. Jamet, A. Mougin, M. Cormier, J. Ferré, V. Baltz, B. Rodmacq, B. Dieny, and R.
 L. Stamps, Phys. Rev. Lett. **99** (21), 217208 (2007).
 49 K. M. D. Hals and A. Brataas, Phys. Rev. B **89** (6), 064426 (2014).

50 D. A. Gilbert, B. B. Maranville, A. L. Balk, B. J. Kirby, P. Fischer, D. T. Pierce, J. Unguris, J. A.
Borchers, and K. Liu, *Nat. Comm.* **6** (2015).
51 R. Tomasello, E. Martinez, R. Zivieri, L. Torres, M. Carpentieri, and G. Finocchio, *Sci. Rep.* **4**, 6784
(2014).
52 O. Heinonen, W. Jiang, H. Somaïly, S. G. Te Velthuis, and A. Hoffmann, *Phys. Rev. B* **93** (9),
094407 (2016).
53 A. L. Balk, C. Hangarter, S. M. Stavis, and J. Unguris, *Appl. Phys. Lett.* **106** (11), 112402 (2015).
54 R. Tomasello, E. Martinez, R. Zivieri, L. Torres, M. Carpentieri, and G. Finocchio, in *Sci. Rep.*
(2014), Vol. 4, p. 6784.

Supplemental material for Simultaneous control of the Dzyaloshinskii-Moriya interaction and magnetic anisotropy in nanomagnetic multilayers

A.L. Balk^{1,2,3}, K-W. Kim^{1,2}, D.T. Pierce¹, M.D. Stiles¹, J. Unguris¹, S.M. Stavis^{1,*}

¹Center for Nanoscale Science and Technology, National Institute of Standards and Technology, Gaithersburg, MD 20899 USA, ²Maryland NanoCenter, University of Maryland, College Park, MD 20742 USA, ³National High Magnetic Field Laboratory, Los Alamos National Laboratory, Los Alamos, NM 87545 USA, *Address correspondence to sstavis@nist.gov

Index:

S1: Sample growth

S2: B_z excitation scheme

S3: Chiral damping

S4: Fitting algorithm

S5: DMI measurement with expanded range

S6: Simultaneous observation of opposite signs of $\mu_0 H_{DMI}$ on the same chip

S7: Auger spectra

References

S1: Sample growth

We sputter Pt/Co/Pt trilayers on a p-type silicon substrate by the following process. First, we perform *in situ* Ar⁺ etching at a power of 50 W for a duration of 120 seconds to remove any contaminants from the substrate. Next, we grow the bottom Pt layer with a base pressure of 5×10^{-4} Pa, a sputtering pressure of 6.6 Pa, and a power of 100 W, which is optimal for film thickness uniformity. Then, we grow the Co layer at a sputtering pressure of 6.6 Pa and a power of 65 W. Finally, we grow the top Pt layer at a sputtering pressure of 6.6 Pa and a power of 60 W. The lower power for growth of the Co and top Pt layers avoids physical damage from atomic and ionic impacts to the existing interfaces of the layers.¹ All sputtering steps use a DC Ar⁺ plasma at a flow rate of $0.83 \text{ atm}\cdot\text{cm}^3\cdot\text{s}^{-1}$. The thickness of the Co layer is $0.8 \text{ nm} \pm 0.1 \text{ nm}$, and the thickness of the top Pt layer is $1.7 \text{ nm} \pm 0.3 \text{ nm}$. We measure the thickness values by growing test wafers under identical sputtering conditions but longer deposition times, and performing atomic force microscopy on the step heights of the test wafers. We propagate uncertainties from the standard uncertainty of the step height measurement. These thickness values correspond to a growth rate of $0.13 \text{ nm}\cdot\text{s}^{-1} \pm 0.02 \text{ nm}\cdot\text{s}^{-1}$ for the Co layer and a growth rate of $0.09 \text{ nm}\cdot\text{s}^{-1} \pm 0.01 \text{ nm}\cdot\text{s}^{-1}$ for the top Pt layer. We obtain X-ray diffraction spectra of the samples, and fit them with a mathematical model based on known parameters of the trilayer to determine the thickness of the bottom Pt film, which is $35 \text{ nm} \pm 2 \text{ nm}$. We conservatively derive the uncertainty of the X-ray

measurement of the bottom Pt film from the uncertainties of the trilayer parameters that we input into the mathematical model, such as interface roughness and thickness of the other layers.

S2: B_z excitation scheme

We use a bipolar, pulsed B_z waveform at a repetition frequency of 50 Hz to 150 Hz and an amplitude of 1 mT to 10 mT to measure magnetic domain bubbles and the effective DMI field $\mu_0 H_{DMI}$ (Fig. S2). Each cycle of the B_z waveform starts with a negative field pulse which saturates the magnetic state of the trilayer. Immediately after the negative field pulse, a smaller positive pulse nucleates and expands bubble domains for measurement. Finally, the magnetic field returns to a small, negative constant field, and remains at that field for bubble observation until the next pulse. The constant negative field ensures complete initialization after each measurement cycle, but is small enough that the domain walls under observation are approximately stationary. The duration of the constant field portion of the waveform is much larger than the total duration of the positive and negative pulses, so the image contrast is close to that of images of stationary bubbles. This B_z waveform allows continuous observation of bubble growth at tens of Hz.

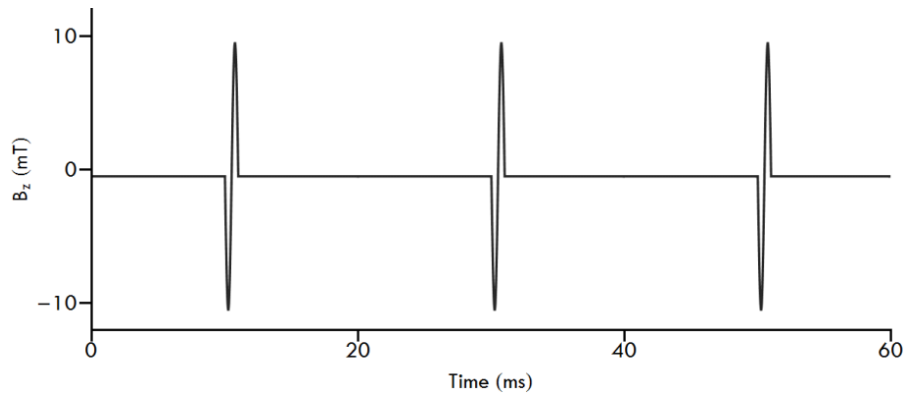


Fig. S2: A simulation of the B_z excitation scheme shows a series of bipolar pulses that first saturate the sample in the negative direction and then drive domain walls for the measurement. The domain walls are approximately stationary during the long constant field portions of the waveform, so the contrast of the video data approaches that of still images of stationary bubbles.

S3: Chiral damping

A recent study² proposed that damping of spin precession, depending on the chirality of the spin texture and separately from the effects of DMI, could lead to a non-zero minimum in domain wall velocity as a function of in-plane field. To investigate this possibility, we plot the domain-wall velocity curves shown in Fig. 2 as a function of B_y , with one curve offset along the x-axis (Fig. S3). If chiral damping were a factor in these measurements, then there would be a clear asymmetry between the two curves, which we do not observe.

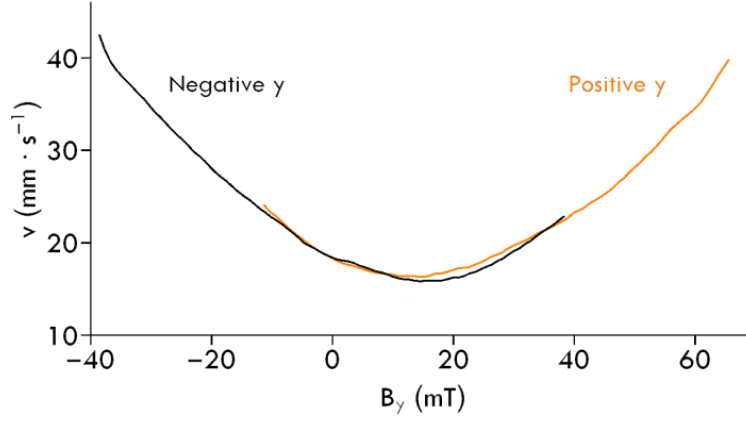


Fig. S3: A damping term which depends on the chirality of the domain wall would manifest as a mismatch between the negative γ domain wall velocity curve (black) and the positive γ domain wall velocity curve which we have offset along the x-axis (orange). We do not observe this mismatch in our data, ruling out the effects of chiral damping in our samples.

S4: Fitting algorithm

Our fitting algorithm determines $\mu_0 H_{DMI}$ from each normalized domain wall velocity (\tilde{v}) curve, (Fig. S4, grey markers) even in the presence of a peak at $B_{y(eff)} = 0$. This peak is present in some of the \tilde{v} curves. The fitting algorithm first fits the $|B_y| < 10$ mT portion of the \tilde{v} curves with a quadratic function to test for the presence of the peak. If this quadratic fit shows a negative second derivative, then the algorithm fits the \tilde{v} curve to the product (Fig. S4, black curve) of a quadratic function (Fig. S4, blue curve) and a sinusoidal function based on the second derivative of the first and second anisotropy energy terms K_1 and K_2 (Fig. S4, red curve). The quadratic function fit determines the measured value of $\mu_0 H_{DMI}$, (Fig S4, vertical black line at $B_{y(eff)} = 3$ mT) and the sinusoidal function models the effect of a changing attempt frequency on the domain wall velocity, as described in the main text. The extracted values of $\mu_0 H_{DMI}$ are insensitive to the model used to describe the central peak. For \tilde{v} curves where the preliminary quadratic fit shows a positive second derivative, the algorithm simply fits the entire trace to a quadratic function to find the value of $\mu_0 H_{DMI}$. Typical uncertainties from these fits are 1 mT, which we determine by propagating the uncertainty of the \tilde{v} curves through the fit.

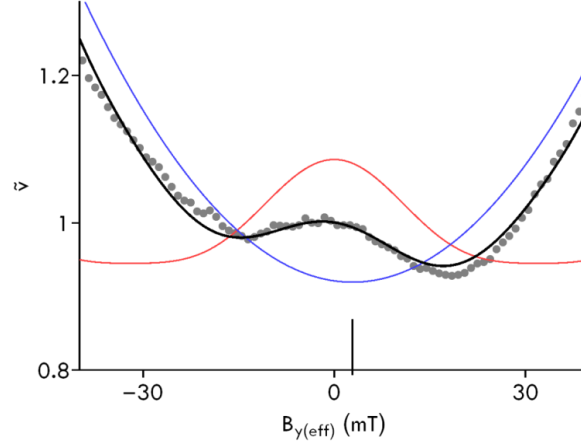


Fig. S4: We use a multistep fitting algorithm to determine the minimum of the quadratic component of the \tilde{v} curves (grey markers). If the curve has a central peak, then we fit the curve to the product of a sinusoidal function derived from the anisotropy constants K_1 and K_2 (red curve) and a quadratic function that models the effect of B_y on the domain wall velocity (blue curve). The minimum of the quadratic function (vertical line at $B_{y(eff)} \approx 0$) determines the parameter $\mu_0 H_{DMI}$.

S5: DMI measurement with expanded range

A surface plot (Fig. S5) shows the DMI field $\mu_0 H_{DMI}$ over the full range of the data taken in this study. This expanded range of data shows that negative $\mu_0 H_{DMI}$ persists to high coercive field $\mu_0 H_C$.

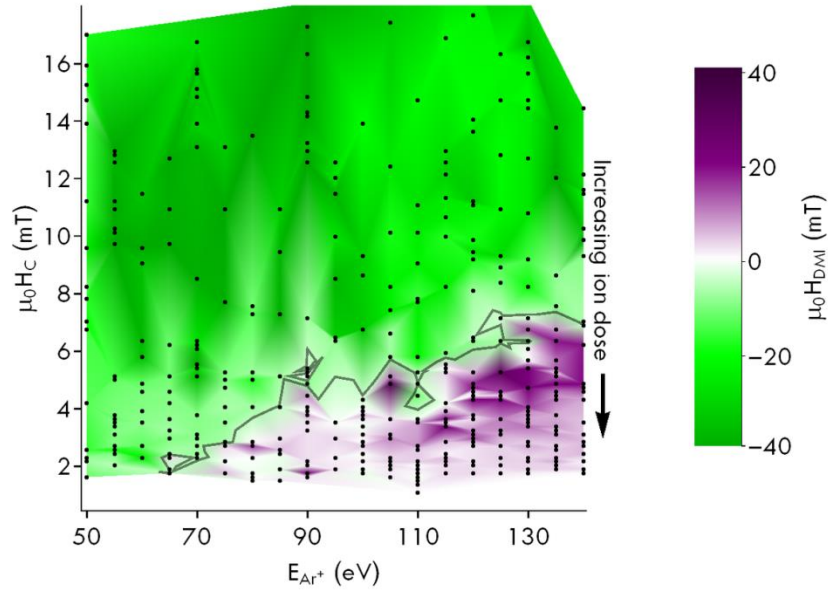


Fig. S5: A surface plot shows the entire set of $\mu_0 H_{DMI}$ values that we measure as a function of $\mu_0 H_C$ and E_{Ar^+} . The gray contour indicates the interpolated boundary between positive and negative $\mu_0 H_{DMI}$. Black markers indicate the measurements upon which the color map is based. Standard uncertainties on

$\mu_0 H_{DMI}$ derived from fits for the data in this plot have a mean value of approximately 1 mT. Uncertainties for the $\mu_0 H_c$ values are less than 0.25 mT, and are determined by the field sampling rate when performing the hysteresis measurements on the film. Uncertainties of the E_{Ar^+} values are less than 1 eV, which we estimate from the uncertainty of the mechanism for energy adjustment of the ion source.

S6: Simultaneous observation of opposite signs of $\mu_0 H_{DMI}$ on the same chip

Supplemental Video S6 shows bubble growth in two regions of the same sample with opposite signs of $\mu_0 H_{DMI}$. We expose the region on the left to 50 eV Ar^+ and the region on the right to 100 eV Ar^+ . We prepare the two regions to have similar $\mu_0 H_c$, enabling simultaneous observation with the same B_z excitation waveform. In this video, the B_z waveform is as we describe in Supplementary S2, such that the growth of the bubbles is invisible but the relative velocity of the domain walls during growth is detectable by their positions in the video. The video is in real time, showing bubbles under exposure to an in-plane triangle B_y field with an amplitude of ≈ 40 mT and a frequency of 1 Hz, in addition to the B_z field. The opposite sign of $\mu_0 H_{DMI}$ for the two regions is evident as the opposite direction of bubble motion in response to the same B_y .

S7: Auger spectra

To verify our explanation of post-growth Ar^+ irradiation as the tuning mechanism of the DMI, we require a technique which can, at least qualitatively, characterize the amount of Pt on the surface of the Co in our trilayers. Auger spectroscopy has the advantages of being surface-sensitive enough to perform this measurement, is non-destructive, and has elemental resolution. Therefore, we perform Auger spectroscopy on areas of the sample irradiated for different durations of 100 eV Ar^+ . We obtain the Auger spectra without exposing the sample to air to avoid atmospheric surface contaminants. After approximately 4 s of Ar^+ irradiation, the Auger spectra exhibit three peaks at energies characteristic of Co (Fig. S7, top, average of all spectra taken in this study). The integrated intensity of these peaks functions as a qualitative indicator of the fraction of Co on the surface of the sample. When plotted as a function of duration of Ar^+ irradiation, (Fig. S7, bottom) the integrated intensity of the peaks shows that the percentage of surface Co increases until approximately 25 s of Ar^+ irradiation, indicating that the top Pt layer is fully etched after that duration. This value matches the etch rate of Pt in response to 100 eV Ar^+ in our chamber, as well as the thickness of the top Pt layer. After taking the Auger spectra, we characterize the perpendicular anisotropy and the DMI on the same areas of the sample as the Auger spectra, to correlate the surface composition with the DMI. The $\mu_0 H_{DMI} = 0$ point occurs before the Co peaks have reached maximum intensity, indicating that the $\mu_0 H_{DMI} = 0$ point occurs after the removal of some, but not all, of the top Pt monolayer. This plot also indicates the duration of Ar^+ exposure at this energy to reach the spin reorientation transition (SRT) of the trilayer.

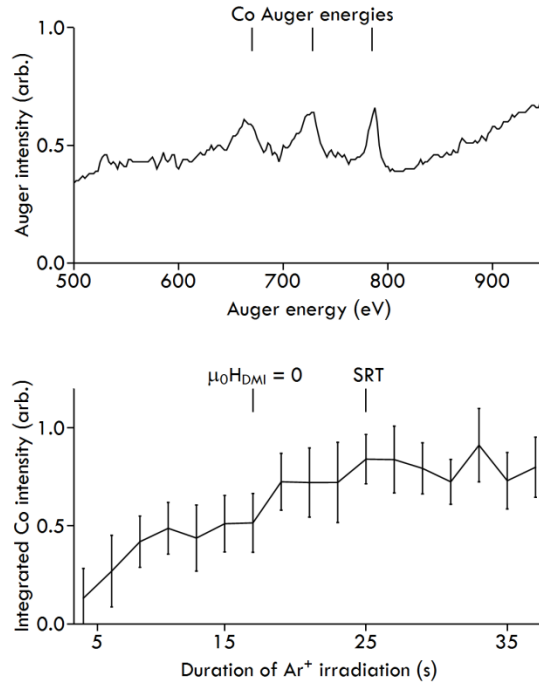


Fig. S7: Auger spectra qualitatively characterize the amount of Co coverage on the surface as a function of duration of irradiation with 100 eV Ar^+ . Top: Three peaks in the Auger energy spectrum indicate the presence of Co in the top 1 nm of material on the sample. This spectrum is the average of all spectra from this Auger study. Typical values of measurement uncertainty for Auger intensity are approximately 0.01, in the arbitrary units of the plot. We estimate this uncertainty as the standard deviation of Auger intensities at regions of the spectra with no evident peaks. Bottom: The integrated intensity of the three peaks indicates the presence of Co in the Auger energy spectrum. The intensity increases above the background at durations of irradiation larger than approximately 5 s, and stops increasing after 25 s of irradiation. The increasing integrated intensity of the Co peaks indicates the removal of the top Pt layer, and coincides with the $\mu_0 H_{\text{DMI}} = 0$ point, which we measure after Auger spectroscopy with magneto-optical Kerr effect microscopy. The SRT tick mark indicates the exposure duration to reach the spin reorientation transition. Vertical bars are standard uncertainties, which we obtain from the spectral values integrated to obtain the data.

References

- 1 P. Carcia, S. Shah, and W. Zeper, *Appl. Phys. Lett.* **56** (23), 2345 (1990).
- 2 E. Jué, C. Safeer, M. Drouard, A. Lopez, P. Balint, L. Buda-Prejbeanu, O. Boulle, S. Auffret, A. Schuhl, A. Manchon, I.M. Miron and G. Gaudin, *Nat. Mater.* **15** (3), 272-277 (2016).